Geophysical Journal International

Geophys J. Int. (2014) **196,** 939–950
Advance Access publication 2013 November 2

doi: 10.1093/gji/ggt407

Real-time magnitude proxies for earthquake early warning in Israel

M. Sadeh, A. Ziv and H. Wust-Bloch

Geophysics and Planetary Sciences, Raymond and Beverly Sackler Faculty of Exact Sciences, Tel-Aviv University, Tel-Aviv, 69978, *Israel.*
E-mail: maytalsadeh@tau.ac.il

Accepted 2013 October 2. Received 2013 October 2; in original form 2013 February 19

SUMMARY

In quest for robust real-time magnitude proxies for earthquake early warning (EEW) in Israel, we use off-line data from 95 earthquakes of magnitudes 2.5–5.3 that were recorded by 25 stations of the Israel Seismic Network between 2003 and 2011. We first examine correlations between the catalogue magnitudes and five different attributes of the early part of the *P* phase, including the low-pass-filtered peak displacement, the peak velocity, the integral of the velocity squared, the predominant period and the characteristic period. We then establish site-specific empirical relations between each proxy and the catalogue magnitude, and infer similar relations for the entire network, after disregarding data recorded at stations for which the site-specific correlation is poor. We find that amplitude-based magnitude proxies are more suitable than frequency-based proxies for rapid magnitude determination, and show that use of site-specific empirical relations between amplitude-based magnitude proxies and catalogue magnitude can increase the accuracy of real-time magnitude estimations. While the present study utilizes off-line data of limited magnitude range, its results clearly indicate that rapid earthquake magnitude determination in Israel and adjacent areas is feasible and can be incorporated effectively into an EEW algorithm.

Key words: Earthquake source observations; Early warning.

1 INTRODUCTION

Earthquake early warning (EEW) algorithms extract real-time information from seismograms, preferentially recorded at stations near the epicentre, and use that information to determine the alert level (Heaton 1985; Nakamura 1988). Once the alert level exceeds some pre-determined threshold, an alert is disseminated to target sites. The further the site is from the epicentre, the longer the interval between the alert notification and the arrival of the strong ground shaking to the target site. Earthquake Early Warning Systems (EEWS) are already operational in Japan, Mexico, Romania, Taiwan and Turkey, and are under test in California, China, Italy and Switzerland (Allen *et al.* 2009). As Israel too is located within an earthquake prone region, the Israeli authorities have decided (June 2012) to implement an EEWS (Allen *et al.* 2012; Hamiel *et al.* 2013).

Earthquake activity in Israel and adjacent areas is associated primarily with the Dead Sea Transform (DST) and the Carmel–Gilboa–Faria System (CFS). The former is an active N–S trending left-lateral transform (Eyal *et al.* 1981; Garfunkel 1981; Joffe & Garfunkel 1987), and the latter is a NW trending left-lateral transtensional fault system that branches out of the former (Ben-Avraham & Ginzburg 1990; Hofstetter *et al.* 1991, Fig. 1). Detailed GPS measurements indicate that the main segments of the DST between the Gulf of Eilat in the South and the Dead Sea, between the Dead Sea and the Sea of Galilee and along the Jordan Fault north of the Sea of Galilee are locked down to a depth of about 10–15 km (Le Beon *et al.* 2008; Al-Tarazi *et al.* 2011; Sadeh *et al.* 2012). Thus, elastic strain along these segments is being currently accumulated. The only segment along which significant aseismic slip may take place is the western strand of the DST in the Dead Sea area (Sadeh *et al.* 2012). Yet, additional data regarding the near fault deformation zone, especially within the Dead Sea basin, is needed for this issue to be resolved. The DST is known to have caused extensive damage and life losses over the past millennia (Ben-Menahem *et al.* 1976; Ambraseys & Karcz 1992; Marco *et al.* 2005; Hamiel *et al.* 2009), and is the main source for earthquake hazard in Israel. Current slip rates along the DST decrease from about 5 mm yr^{-1} south of the DST–CFS intersection to 3.8 mm yr^{-1} north of it (Sadeh *et al.* 2012). This displacement rate decrease is due to slip transfer from the DST to the CFS, whose left-lateral and extension rates amounts to 0.6–0.7 mm yr^{-1} (Sadeh *et al.* 2012). Despite these rates being very small, the possibility of moderate-to-large earthquakes along that system cannot be discounted (a magnitude 5.3 occurred near the Carmel Fault in 1984). Thus, the available GPS data together with the proximity of the CFS northern end to Haifa and major petrochemical facilities suggest that the seismic risk along the CFS is high.

Distances between major population centres in Israel and seismically active faults are very short. For example, Jerusalem is located just 25 km away from the Kalia Fault, the site of a damaging (*M* 6.2) earthquake in 1927 (Shapira *et al.* 1993). It is mainly because of these short distances and the destructive potential of *S* waves

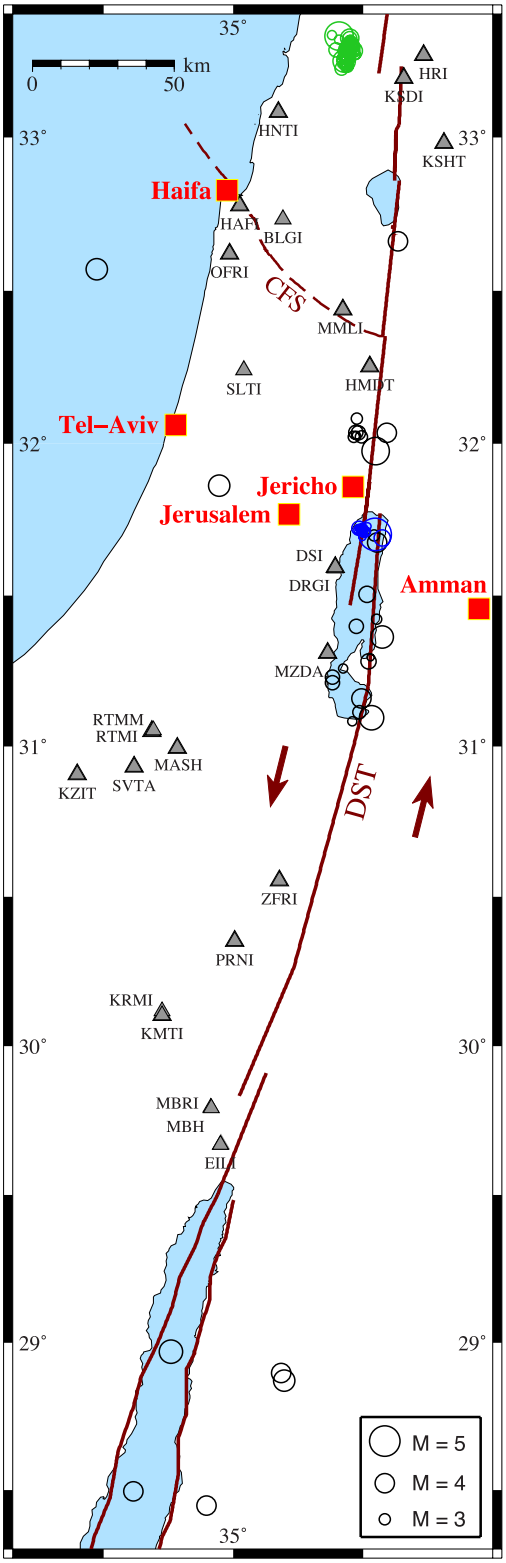

Figure 1. Location map showing the 95 hypocentres listed on Table S1 (circles), with green and blue circles indicating earthquakes belonging to the 2008 Southern Lebanon swarm and the 2004 Dead Sea aftershock sequence, respectively, and the black circles indicating events that occurred along the DST between 2003 and 2011. The triangles denote the 25 GII stations that recorded the data used in this study. The Dead Sea Transform (DST) and the Cramel–Faria System (CFS) are indicated by solid and dashed lines, respectively.

that it would be most useful if rapid earthquake magnitude determination for EEW in Israel could be done using the part of the seismic signal that precedes the *S*-wave arrival. Clearly, reducing the length of the pre-*S*-wave signal to its minimum may save critical warning time. Thus, the challenge consists in determining what is the shortest interval that contains essential source information. Several researchers have reported meaningful correlation between the duration of the slow initial phase (SIP) of the seismic signal and the ultimate event size, with the duration of the SIP being very short compared to the total rupture duration (e.g. Iio 1992; Ellsworth & Beroza 1995; Iio 1995; Beroza & Ellsworth 1996). While the implications of this result to earthquake mechanics are debatable, it is clear that the incorporation of the SIP duration into EEWS is unfeasible. Both the correlation of the SIP duration with earthquake magnitude (e.g. Lewis & Ben-Zion 2007), and its picking by automatic routines are not sufficiently robust for EEW applications. Thus, the early portion of the seismograms used for EEW applications should be extended to time windows that are longer than those considered in the aforementioned SIP studies. Studies that considered longer intervals (2–4 s) established meaningful empirical correlations between earthquake magnitude and different attributes of the early portion of seismic signals. These include the low-pass-filtered peak displacement (Wu & Zhao 2006; Zollo *et al.* 2006) and peak velocity (Wurman *et al.* 2007), the integral of the velocity squared (Festa *et al.* 2008) and the signal's frequency content (predominant period: Nakamura 1988; Allen & Kanamori 2003; characteristic period: Wu & Kanamori 2005). In fact, these parameters are already incorporated into worldwide EEWS that are currently under test or are operational.

The result that the SIP duration scales with earthquake magnitude and the notion that the SIP reflects the final stage of the nucleation phase have led to the suggestion that the rupture process is deterministic, with similar characteristic length and timescale controlling both its initiation and arrest (Ellsworth & Beroza 1995; Iio 1992, 1995; Beroza & Ellsworth 1996). Additional support for this idea comes from predominant frequency analysis of South California earthquakes, suggesting that the rupture size can be estimated before the cessation of the rupture (Olson & Allen 2005). While the question as to whether the rupture process is deterministic is still under debate (Olson & Allen 2006; Rydelek & Horiuchi 2006), it is agreed that ground motion analysis of the first 2–4 s of the seismic signal may at least constrain the minimum magnitude.

As the slip rate accommodated by the DST is relatively low ($\sim$5 mm yr^{-1}), so is the rate of earthquake activity. At the current level of seismicity, a magnitude 5 occurs on average once every 10 yr. The most recent destructive earthquake that struck the region is a magnitude 6.2, which ruptured in the Jericho area in 1927 and resulted in a few hundred casualties (Avni 1999). The Israel Seismic Network (ISN) became operational during the mid-1980s. It consists of 20–30 short period and broad-band velocity metres and a few dozens of accelerometers. Owing to the low seismicity rate, the shortness of the instrumental recording and the sparseness of the ISN, the data set that is available for seismological research in Israel is rather limited. Preliminary warning time simulations indicate that for EEWS to be implemented successfully in Israel, the existing ISN has to be upgraded and densified, a large number of strong-motion instruments have to be deployed along the major faults and the communication latencies must be reduced (Allen *et al.* 2012; Hamiel *et al.* 2013).

The main objective of this study is to identify a set of robust real-time magnitude proxies for EEW in Israel and adjacent areas. To this end we examine correlations between off-line catalogue

magnitudes and five different attributes of the early part of the *P* phase. In order to identify problematic stations, we first examine these correlations at each station separately. Next, after disregarding data recorded at stations for which the site-specific correlation is poor, we establish network-average empirical relations between the *P*-wave attributes and the catalogue magnitude. We show that use of site-specific empirical relations reduces the effect of local biases, such as site effect and instrumental response, and improves the magnitude assessment. Finally, we discuss the implications of the results on the prospects of an onsite EEWS along the DST.

2 DATA AND METHOD

2.1 Data selection and processing

We selected waveforms of 95 earthquakes that were recorded by 25 of the ISN seismometers (grey triangles in Fig. 1) and archived by the seismology division of the Geophysical Institute of Israel (GII; Table S1). Out of these, 62 earthquakes belong to two distinct clusters; the first includes the 2004 February 11, M_w 5.3, Northern Dead Sea earthquake, and 14 of its aftershocks (blue circles in Fig. 1), and the second consists of the 2008 earthquake swarm that occurred near the town of Tzor in south Lebanon (green circles in Fig. 1). The remaining 32 earthquakes occurred along the DST between 2003 and 2011 (black circles in Fig. 1). The duration magnitudes reported in the ISN catalogue range between 2.5 and 5.2 (M_w is not reported in the ISN catalogue).

We manually picked *P*-phase arrivals and low-pass filtered the velocity seismograms at 3 Hz. Several researchers high-pass the data at 0.075 Hz in order to lessen the possible effect of low-frequency noise on the signal's frequency content and minimize the error that such noise may introduce into the displacement time-series calculation (e.g. Wu & Kanamori 2005). However here, because seismograms having low signal-to-noise ratio (SNR) were not admitted to our data set and since we only start integrating the velocity time-series at the time of the *P*-wave picking, such filtering is not required. Since many of the seismometers available for this study are single-component, we only used the vertical-component records. We limited our analyses to source–receiver distances of 200 km, and calculated real-time magnitude proxies using the first 3 s of the *P* phase. Using a time window shorter than 3 s resulted in greater errors, and increasing the time window beyond that did not seem to improve the magnitude estimate. Within 3 s, the rupture front is expected to propagate at least 7.5 km, thus breaking a fault patch corresponding to a magnitude 6.1 (Wells & Coppersmith 1994). As the largest earthquake in our data set is of magnitude 5.2, all ruptures considered in this study ceased to grow well before the 3-s-long time window ended. For receiver–source distances below 25 km, such a time window may be 'contaminated' by some *S*-phase energy. To exclude *S* phases, we assessed the *S*-minus-*P* interval, and shortened the time window if that interval is less than 3 s. In assessing the *S*-minus-*P* interval we followed a simple (and conservative) rule of thumb of adding 1 s per 8 km of hypocentral distance (Wurman *et al.* 2007). This moveout correction was applied to 19 (out of 720) seismograms, most of which were recorded at stations DRGI and DSI. Owing to the poor station coverage and the asymmetric station–source configuration (i.e. lack of stations east of the DST and north of the S. Lebanon swarm), hypocenteral depths are poorly constrained. Thus, in calculating the hypocentral distances, we disregarded the ISN catalogue depth and used a fixed depth of 8 km.

2.2 Real-time magnitude proxies

In quest for real-time magnitude proxies, we examine correlations between the ISN catalogue magnitude and five different attributes of the *P* phase. These magnitude proxies may be categorized into amplitude- and frequency-based quantities.

2.2.1 Amplitude-based proxies

The assessment of proxies belonging to the amplitude-based category requires a distance correction, and therefore can only be used in conjugation with real-time source–receiver distance determination. We rescaled the measured particle velocities to an arbitrary reference distance, R_{ref}, by multiplying each seismogram by R/R_{ref}, where R is the hypocentral distance, and throughout this study we use $R_{ref} = 100$ km. A plot of the logarithm of the distance-corrected peak absolute velocity during the first 3 s of the *P* phase as a function of the hypocentral distance shows that, despite its simplicity, this distance correction successfully accounts for the velocity attenuation due to geometrical spreading, and suggests that attenuation due to anelasticity is unimportant for the distance ranges considered here (Fig. 2).

Peak displacement, *Pd*: Previous researchers have established empirical relations between the logarithm of the distance-corrected peak displacement and the magnitude (Wu & Kanamori 2005; Zollo *et al.* 2006). We obtain displacement time-series by integrating distance-corrected velocity seismograms, and find the maximum absolute value for the first 3 s of the waveform according to:

$$Pd = \max\left[\mathrm{abs}\left(\int_{t_0}^{t_0+\Delta t} v_R \, \mathrm{d}t\right)\right], \quad (1)$$

where v_R is the distance corrected particle velocity, t_0 is the time of the first picking, Δt is an interval of 3 s and the 'max' and 'abs' signify 'maximum' and 'absolute' values, respectively.

Peak velocity, *Pv*: It is instructive to compare the accuracies of real-time magnitude estimates that are based on *Pd* with those based on *Pv*, since the numerical integration of velocity seismograms to displacement may introduce errors into the *Pd* estimate, and since

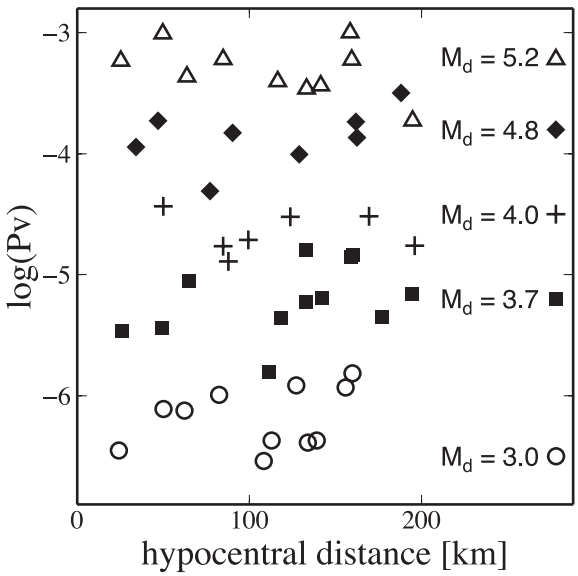

Figure 2. The logarithm of the distance-corrected peak velocity as a function of the hypocentral distance for a selection of five earthquakes. The peak velocity is rescaled with respect to a reference distance of 100 km.

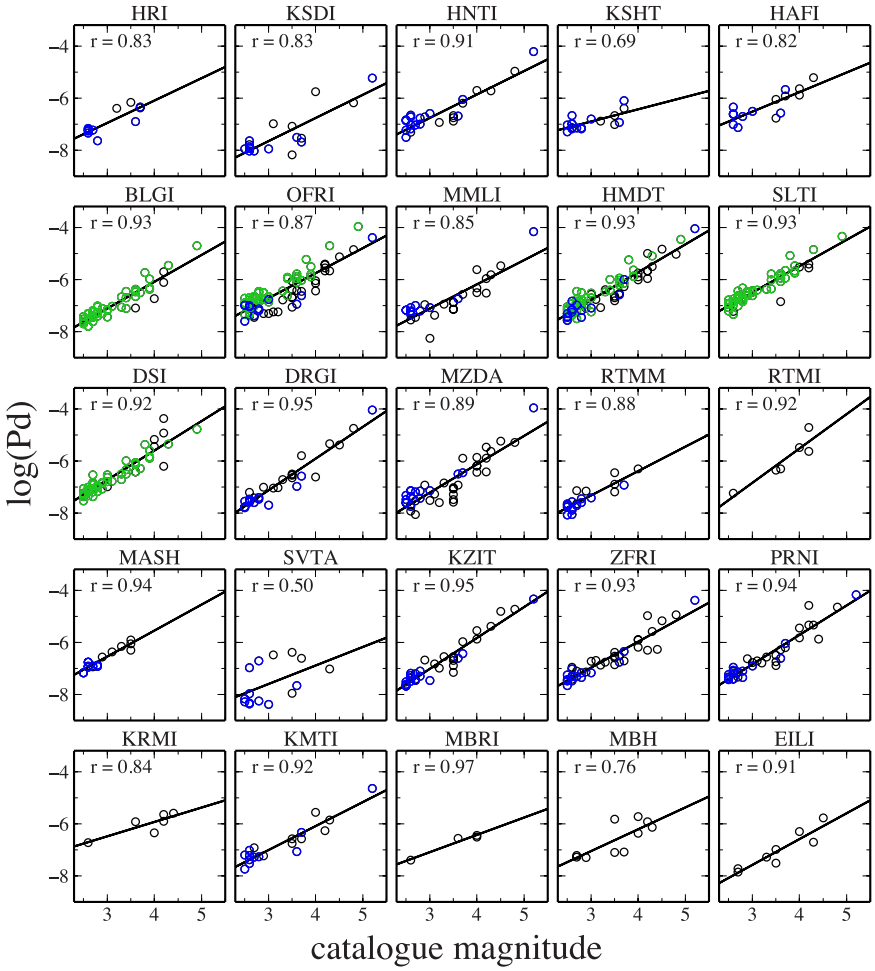

Figure 3. The logarithm of *Pd* as a function of the catalogue magnitude (*Md*) at individual stations. Green and blue symbols indicate earthquakes belonging to the 2008 Southern Lebanon swarm and the 2004 Dead Sea aftershock sequence, respectively, and the black symbols indicate events that occurred along the DST between 2003 and 2011. The solid lines are the linear least-square fit, with the correlation coefficient indicated at the top-left corner of each panel.

there is no obvious reason why Pv should be less well correlated with the catalogue magnitude than Pd. The Pv is calculated according to:

$$Pv = \max[\mathrm{abs}(v_R(t))],\ t_0 \le t \le t_0 + \Delta t. \tag{2}$$

Integral of the velocity squared, $IV2$: Introduced by Festa *et al.* (2008), this parameter is defined as:

$$IV2 = \int_{t_0}^{t_0+\Delta t} v_R^2\, \mathrm{d}t. \tag{3}$$

Both Festa *et al.* (2008) and Lancieri *et al.* (2011) reported a stable correlation between the logarithm of $IV2$ and the catalogue magnitude over a wide magnitude range.

2.2.2 *Frequency-based proxies*

The rational behind the frequency-based real-time magnitude proxies is simple; because the frequency content of the initial ground motion caused by large earthquakes is richer in low frequencies than that caused by small earthquakes (Aki 1967), earthquake magnitude should scale with the dominant and/or the average period of the initial ground motion (Nakamura 1988). The main advantage of the frequency-based proxies with respect to their amplitude-based counterparts is that the former need not be corrected for the source–receiver distance.

Predominant period, τ_p: Calculated recursively according to Nakamura (1988) and Allen & Kanamori (2003):

$$\tau_p = \max(2\pi\sqrt{V_n/D_n}), \tag{4}$$

where $V_n = \alpha V_{n-1} + v_n^2$ and $D_n = \alpha D_{n-1} + (\mathrm{d}v_n/\mathrm{d}t)^2$. The 'max' stands for 'maximum value', n is a time index, v is the recorded particle velocity, V is the smoothed particle velocity squared, D is the smoothed acceleration and α is a smoothing coefficient, whose value is slightly less than a unity (we use $\alpha = 0.99$).

Characteristic period, τ_c: Proposed by Wu & Kanamori (2005), it is defined as:

$$\tau_c = 2\pi\sqrt{\frac{\int_{t_0}^{t_0+\Delta t} u^2 \mathrm{d}t}{\int_{t_0}^{t_0+\Delta t} v^2 \mathrm{d}t}}, \tag{5}$$

where u is the ground displacement.

Wolfe (2006) pointed out that the above proxies are nonlinearly dependent on the spectral amplitude and the frequency in a manner that overweight the highest frequencies in the spectrum, and showed that use of eqs (4) and (5) introduces errors into this parameter. Shieh *et al.* (2008) have shown that τ_p is more sensitive than τ_c to the

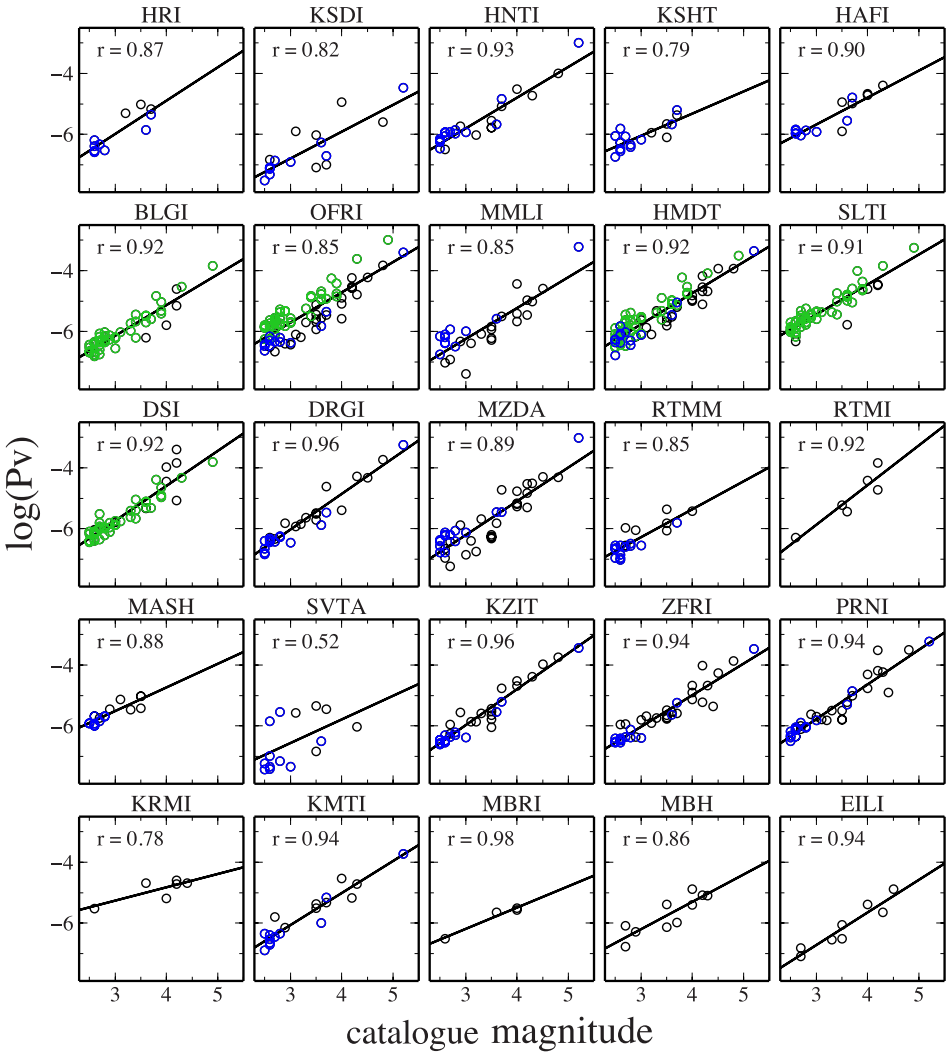

Figure 4. The logarithm of *Pv* as a function of the catalogue magnitude (*Md*) at individual stations. Green and blue symbols indicate earthquakes belonging to the 2008 Southern Lebanon swarm and the 2004 Dead Sea aftershock sequence, respectively, and the black symbols indicate events that occurred along the DST between 2003 and 2011. The solid lines are the linear least-square fit, with the correlation coefficient indicated at the top-left corner of each panel.

pre-signal noise level. Here, in an attempt to lessen the effect of noise, we disregard the first 0.5 s of the signal.

3 EMPIRICAL RELATIONS BETWEEN REAL-TIME MAGNITUDE PROXIES AND CATALOGUE MAGNITUDE

We use the following expression to establish empirical relations between each of the five real-time magnitude proxies and the catalogue magnitude:

$$\log(\mathrm{MP}) = A + B \cdot M_d,$$

where 'MP' stands for 'magnitude proxy', M_d is the duration magnitude listed on the ISN catalogue and A and B are the linear regression coefficients. We first determine the log (MP) versus M_d relations at each station separately, and use the correlation coefficient to assess the strength of that relation. We then establish this relation for the entire network, excluding those stations for which the correlation coefficient is low. Owing to the large scattering of the frequency-based proxies versus magnitude at individual stations, meaningful site-specific empirical relations can only be established for the amplitude-based proxies.

3.1 Site-specific empirical relations

The logarithm of *Pd*, *Pv* and *IV*2 as a function of the catalogue magnitude at individual stations are shown in Figs 3–5, with data belonging to different earthquake clusters shown in different colours, and the solid black lines are the linear regression lines of the entire data set recorded at each station. The correlation coefficients in most stations (indicated at the top-left corner of each panel in Figs 3–5) exceed 0.85, indicating that *Pd*, *Pv* and *IV*2 may serve as robust real-time magnitude proxies. Although *Pd* is the magnitude proxy favoured by currently adopted EEW algorithms, our results indicate that the *IV*2 proxy outperforms *Pd*, since the correlation of the former with the catalogue magnitude is larger than that of the latter in 17 out of the 25 stations (the linear regression coefficients and the correlation coefficients are summarized in Table 1). While the correlations between site-specific amplitude-based proxies and catalogue magnitude are strong at most stations,

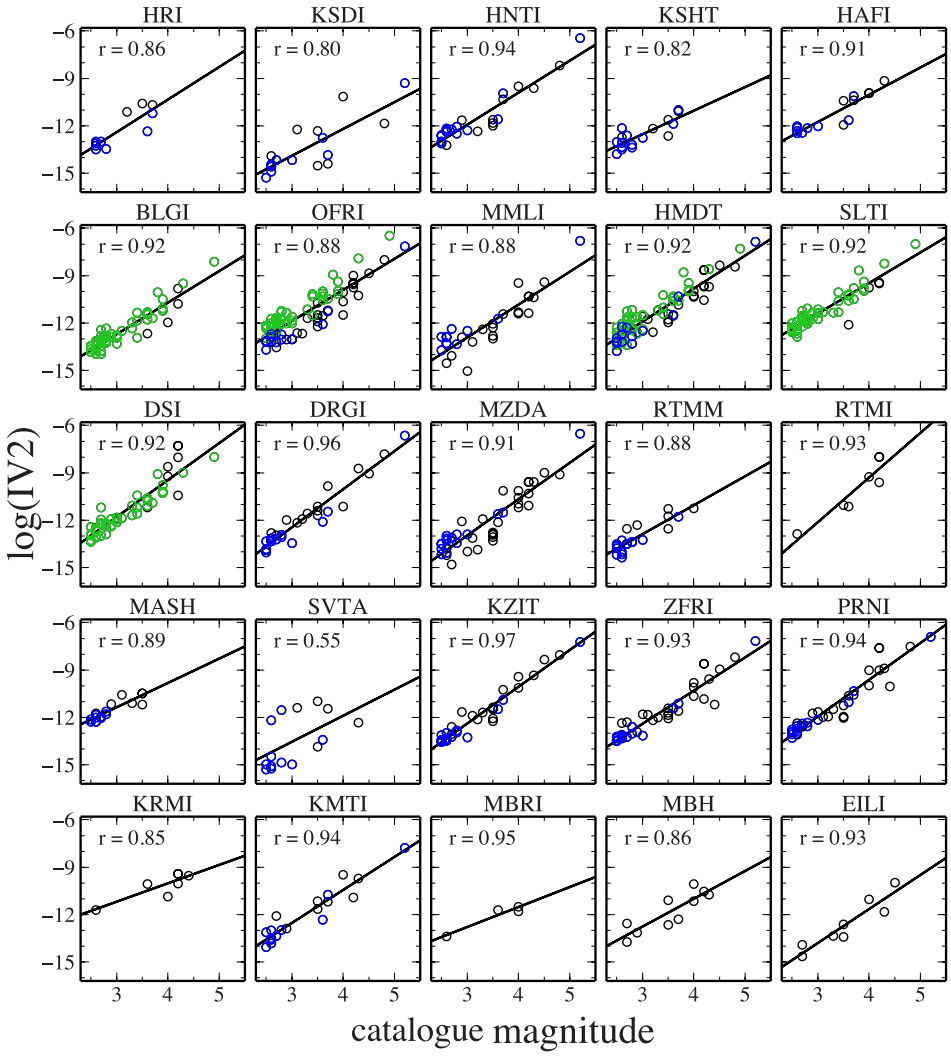

Figure 5. The logarithm of *IV*2 as a function of the catalogue magnitude (*Md*) at individual stations. Green and blue symbols indicate earthquakes belonging to the 2008 Southern Lebanon swarm and the 2004 Dead Sea aftershock sequence, respectively, and the black symbols indicate events that occurred along the DST between 2003 and 2011. The solid lines are the linear least-square fit, with the correlation coefficient indicated at the top-left corner of each panel.

those between site-specific frequency-based proxies and magnitude are poor throughout the network (Figs S1 and S2).

Some of the highly correlated site-specific empirical relations are based on a statistically meaningful sample that spans a (relatively) wide magnitude range (e.g. BLGI, HMDT, SLTI and KZIT), whereas others suffer from insufficient sample (e.g. MBRI) and/or a narrow magnitude range (e.g. MASH). Commonly, these problems are addressed by data stacking and use of a single network-average empirical relation.

3.2 Network-average empirical relation

The logarithm of *Pd*, *Pv* and *IV*2 (empty symbols) as a function of the catalogue magnitude are shown in Fig. 6. Excluded from these diagrams are the three stations (KSDI, KSHT and SVTA) for which the correlation coefficients of the site-specific linear regressions are less than 0.85 (Table 1). In the previous section, we presented the results of a site-specific analysis, which shows that the *IV*2 proxy is outperforming the other two. Here, however, the correlation coefficients of the three linear regressions are nearly equal ($r \sim 0.85$), suggesting that the three network-averaged proxies are performing similarly well.

In addition to the linear regression lines of the entire data set (in black), we show the linear regression lines of the two earthquake clusters separately. Note that the linear regression lines corresponding to the 2008 South Lebanon swarm (in green) are shifted upwards with respect to those corresponding to the 2004 Dead Sea aftershock sequence (in blue). While the dissimilarity of linear regression lines corresponding to geographically distinct earthquake clusters may be indicative of path effects on the magnitude proxies, we suspect that these shifts are due to the network being un-calibrated between 2004 and 2007.

The logarithm of τ_c and τ_p as a function of the catalogue magnitude are shown in Fig. 7. For each event we computed the median of the magnitude proxy (solid symbols), and used these medians to obtain a network-average linear regression line for each magnitude proxy (black lines). Here too we exclude the three stations for which the correlation coefficients of the site-specific linear regressions are less than 0.85 (Table 1). Note the large scattering of the data with respect to the linear regression lines, and that τ_p is slightly better correlated with the magnitude than τ_c is. Previous

Table 1. Linear regression parameters and correlation coefficients obtained for each of the three amplitude-based magnitude proxies. Bold fonts are used to indicate the largest correlation coefficient at each station.

	N	*Pd*			*Pv*			*IV*2		
Site	events	A	B	*r*	A	B	*r*	A	B	*r*
					Network-average					
	95	−10.031	1.041	0.864	−8.933	1.010	0.848	−18.425	2.061	0.860
					Site-specific					
HRI	11	−9.538	0.859	0.830	−9.286	1.097	**0.874**	−18.600	2.062	0.862
KSDI	17	−10.321	0.890	**0.831**	−9.432	0.880	0.825	−19.000	1.697	0.807
HNTI	25	−9.454	0.898	0.912	−8.826	1.007	0.937	−18.026	2.030	**0.940**
KSHT	17	−8.318	0.471	0.695	−8.238	0.729	0.793	−17.024	1.493	**0.825**
HAFI	15	−8.785	0.753	0.821	−8.335	0.886	0.901	−16.918	1.719	**0.916**
BLGI	49	−10.195	1.028	**0.932**	−9.167	1.009	0.924	−18.707	1.999	0.926
OFRI	84	−9.600	0.961	0.871	−8.699	0.996	0.859	−17.822	1.978	**0.882**
MMLI	29	−9.922	0.934	0.858	−9.287	1.014	0.857	−19.158	2.081	**0.883**
HMDT	80	−9.986	1.065	**0.935**	−8.830	1.023	0.921	−18.186	2.092	0.927
SLTI	52	−9.550	1.014	**0.932**	−8.404	0.987	0.920	−17.219	1.934	0.927
DSI	53	−10.126	1.131	0.928	−9.173	1.145	**0.929**	−18.827	2.340	0.925
DRGI	29	−10.789	1.219	0.958	−9.551	1.174	0.962	−19.703	2.415	**0.963**
MZDA	41	−10.484	1.089	0.894	−9.552	1.113	0.890	−19.868	2.298	**0.913**
RTMM	20	−10.147	0.939	**0.888**	−9.032	0.917	0.858	−18.409	1.839	0.883
RTMI	6	−10.812	1.320	0.923	−9.792	1.306	0.923	−20.615	2.831	**0.930**
MASH	17	−9.541	0.996	**0.944**	−7.843	0.776	0.884	−15.999	1.542	0.891
SVTA	15	−9.733	0.711	0.503	−8.892	0.775	**0.523**	−18.488	1.649	0.551
KZIT	33	−10.583	1.187	0.958	−9.533	1.184	0.965	−19.377	2.330	**0.970**
ZFRI	38	−9.965	0.997	0.934	−9.137	1.038	**0.942**	−18.699	2.100	0.939
PRNI	36	−10.241	1.130	0.947	−9.195	1.138	0.947	−18.919	2.322	0.947
KRMI	6	−8.132	0.550	0.842	−6.588	0.441	0.788	−14.667	1.162	**0.850**
KMTI	19	−9.765	0.918	0.927	−9.215	1.050	0.948	−18.803	2.089	**0.949**
MBRI	4	−9.076	0.662	0.976	−8.290	0.699	**0.982**	−16.587	1.266	0.959
MBH	10	−9.582	0.842	0.769	−8.897	0.898	**0.868**	−18.073	1.768	0.863
EILI	8	−10.549	0.990	0.919	−9.934	1.071	**0.948**	−20.271	2.154	0.931

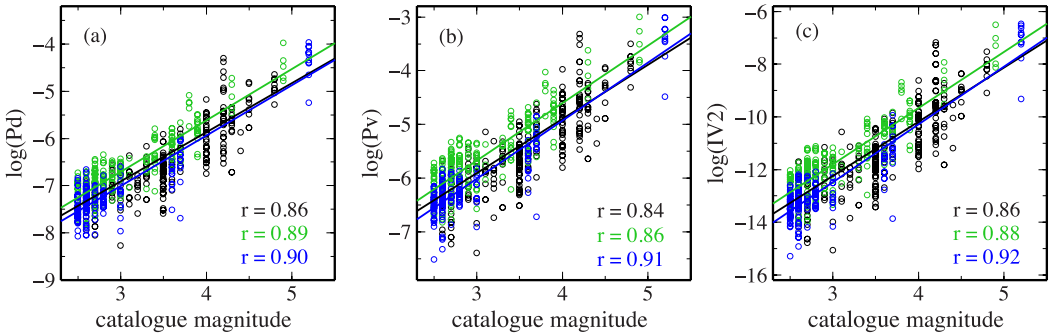

Figure 6. Correlations between amplitude-based magnitude proxies and catalogue magnitude (*Md*). (a) *Pd* as a function of catalogue magnitude. (b) *Pv* as a function of catalogue magnitude. (c) *IV*2 as a function of catalogue magnitude. Each point represents a measurement at an individual station. Green and blue symbols indicate earthquakes belonging to the 2008 Southern Lebanon swarm and the 2004 Dead Sea aftershock sequence, respectively, and the black symbols indicate events that occurred along the DST between 2003 and 2011. The solid green, blue and black lines are the linear least-square fits corresponding to the Lebanese swarm, the Dead Sea sequence and the entire data set, respectively, with respective correlation coefficients indicated at the bottom-right corner of each panel.

researchers that calibrated frequency-based magnitude proxies used data sets that span four or more magnitude units, with the smallest magnitude being greater than 3 (Allen & Kanamori 2003; Lockman & Allen 2005; Wu & Kanamori 2005). Unfortunately, owing to the low seismicity rate and the shortness of the instrumental catalogue, the data that are available for this study span less than three magnitude units with the smallest magnitude being equal to 2.5. Given the limited magnitude range, we conclude that amplitude-based magnitude proxies are more suitable than the frequency-based proxies for rapid magnitude determination in Israel and adjacent areas, and thus only the amplitude-based proxies are considered further on.

4 RAPID MAGNITUDE DETERMINATION

The empirical relations between each of the three amplitude-based magnitude proxies and the catalogue magnitude are now being used for magnitude determination.

4.1 Network-average versus site-specific empirical relations

Some of the scattering in the log (MP) versus M_d plots of Fig. 6 may be due to differences in site effect, instrument response and the instruments being uncalibrated. The effect of such site-specific

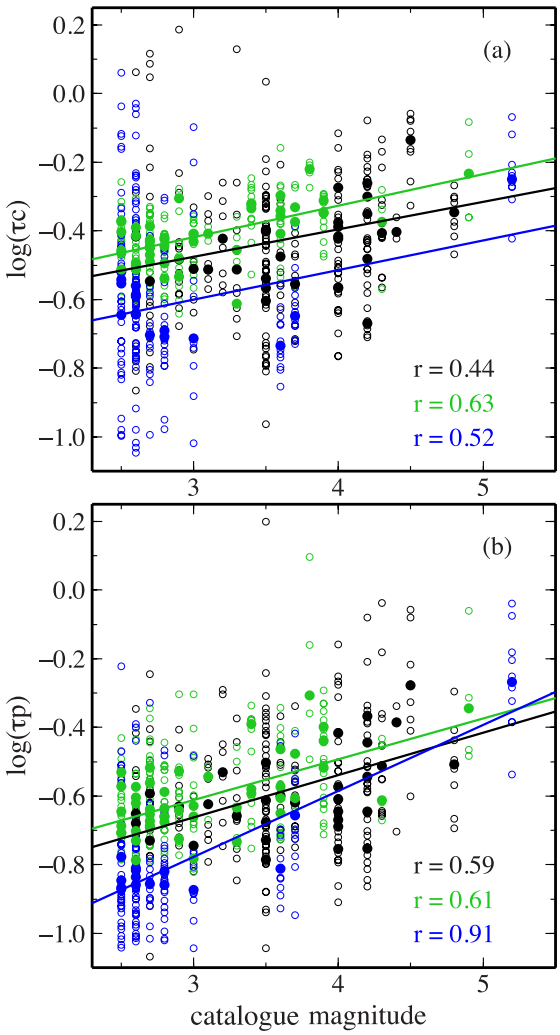

Figure 7. Correlations between frequency-based magnitude proxies and catalogue magnitude (*Md*). (a) τ_c as a function of catalogue magnitude. (b) τ_p as a function of catalogue magnitude. Green and blue symbols indicate earthquakes belonging to the 2008 Southern Lebanon swarm and the 2004 Dead Sea aftershock sequence, respectively, and the black symbols indicate events that occurred along the DST between 2003 and 2011. Open and solid symbols indicate individual measurement and event median values, respectively. The solid green, blue and black lines are the linear least-square fits to the solid symbols corresponding to the Lebanese swarm, the Dead Sea sequence and the entire data set, respectively, with respective correlation coefficients indicated at the bottom-right corner of each panel.

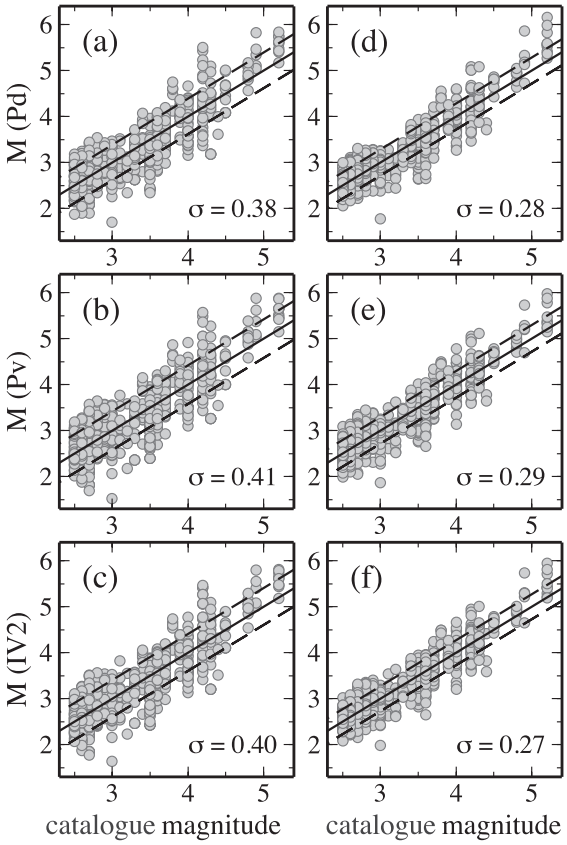

Figure 8. Comparison between magnitude estimates using the network-average (left-hand column) and the site-specific (right-hand column) empirical relations. Real-time magnitude estimates as a function of catalogue magnitude (*Md*), with each point representing a magnitude estimate using a 3-s-long *P*-phase waveform recorded at an individual station. The solid lines indicate 1:1 relation and the dashed lines indicate the 1σ uncertainty.

biases on the rapid magnitude determination may be lessened by applying site-specific empirical relations. We now examine the extent to which use of site-specific empirical relations may improve the accuracy of the rapid magnitude determination.

We use the amplitude-based network-average empirical relations to determine the magnitude of event *i* at station *j* according to

$$M_{ij}^{\text{network}}(\text{MP}) = \frac{\log \text{MP}_{ij} - A(\text{MP})}{B(\text{MP})}, \quad (6)$$

and use the site-specific empirical relations according to

$$M_{ij}^{\text{site}}(\text{MP}) = \frac{\log \text{MP}_{ij} - A_j(\text{MP})}{B_j(\text{MP})}. \quad (7)$$

Inspection of M_{ij}(MP) versus M_d resulting from the two approaches (Fig. 8) reveals that the site-specific magnitude estimates are more accurate than the network-average estimates; while use of eq. (6) yields standard deviation of ∼0.4, use of eq. (7) yields standard deviations smaller than 0.3. Since at this stage of the EEWS development there is still no clear definition of what a true alarm is, the number of false and missed alarms in our data set cannot be determined. If, for example, a true alarm would be regarded as any $M \geq 5.5$, our data set contains three false alarms if the network-average approach is to be implemented, and up to two false alarms if the site-specific approach is implemented.

The data presented in Fig. 8 and the data used for the inference of the empirical relation are identical. It is, however, preferable to evaluate the performance of the magnitude proxies using an independent data set. Thus here, despite the limited data set, we test the performance of the network-average magnitude determination approach on a subset of the data that is excluded from the calculation of the log (MP) versus M_d relation. We randomly selected about 75 per cent of the earthquakes, ensuring that this percentage remains nearly constant across the magnitude range that is spanned by the data (black symbols in Fig. 9), and inferred a log (MP) versus M_d relation to that subset. Next, we used that relation to predict the magnitude of the remaining 25 per cent (grey symbols in Fig. 9). Judging from the error standard deviation of the predicted versus catalogue magnitudes, we conclude that real-time magnitude assessment meets the standards of other regional EEWS (Böse *et al.* 2013).

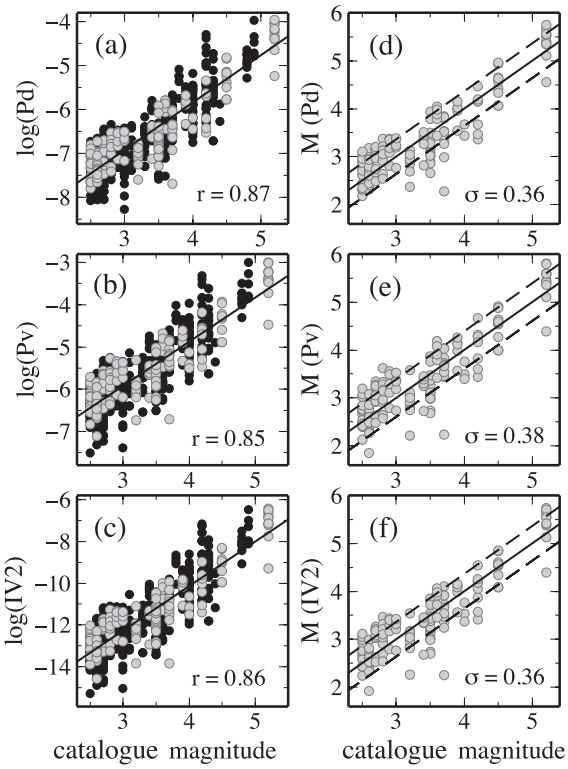

Figure 9. Results of the independent data test. Earthquakes used for the inference of the network-average log (MP) versus *Md* relations are indicated by the black symbols, and the independent data set used for testing the magnitude prediction are indicated by the grey symbols. (a–c) The three amplitude-based magnitude proxies as a function of the catalogue magnitude, with the solid lines indicating the least-squares fits to the black symbols. (d–f) Real-time magnitude estimates as a function of catalogue magnitude, with solid and dashed lines indicating the 1:1 relation and the 1σ uncertainty, respectively.

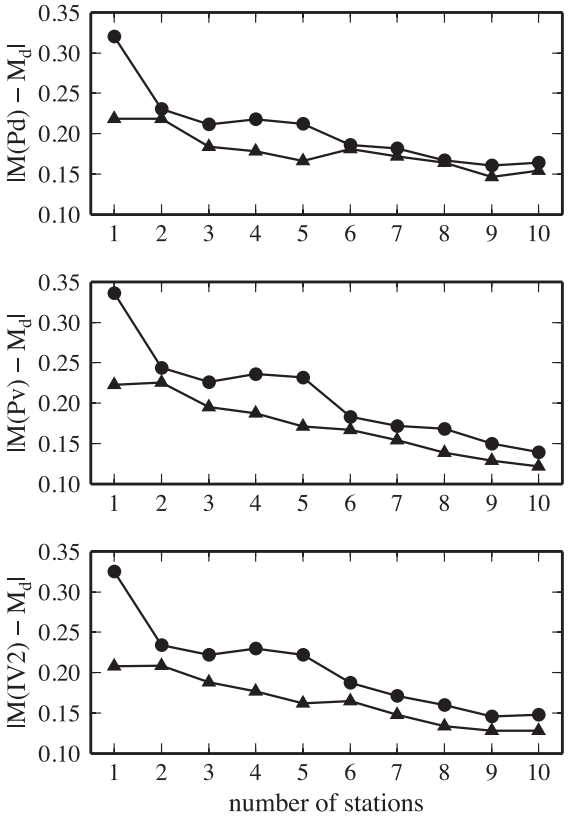

Figure 10. Average absolute magnitude discrepancy (with respect to the catalogue magnitude) as a function of the number of stations providing *P*-wave data. Magnitude discrepancies resulting from the application of the network-average and the site-specific empirical relations are indicated by circles and triangles, respectively.

To further assess the performances of the site-specific approach with respect to the network-average approach, we examine how the magnitude estimate error changes with increasing number of *P*-wave records. The average discrepancy between the real-time magnitude estimates and the catalogue magnitudes as a function of stations are shown in Fig. 10. Using eq. (6), the average magnitude discrepancy decreases from 0.3–0.35 using one station to 0.2–0.25 using two stations, and it drops more gently beyond that point. Using eq. (7) the average magnitude discrepancy is less than 0.25 from the very first station, and it drops almost constantly with increasing the number of recording stations. In conclusion, magnitude errors using the site-specific approach are slightly smaller than those resulting from application of the network-average empirical relations, and the three amplitude-based magnitude proxies are performing similarly well.

4.2 Example timeline

The 2004 February 11, M_w 5.3, Northern Dead Sea earthquake, is the strongest earthquake within the study area since 1995. The average magnitude error as a function of time with respect to its origin time (time of *P*-wave picking plus 3 s) is shown in Fig. 11 for the network-average (circles) and the site-specific (triangles) approaches. Using the catalogue epicentral distance for rescaling the velocity seismograms, we find that the magnitude discrepancies resulting from the network-average approach are equal to 0.45–0.6 up to the third station, and decrease thereafter, reaching to about 0.4 after the 10-th trigger.

The first and third triggers occurred at stations DSI and HMDT, respectively, where the ground shaking amplitude is strongly correlated with earthquake magnitude, whereas the second and fourth triggers occurred at stations MZDA and MMLI, where the ground shaking is less well correlated with the magnitude. Consequently, the magnitude discrepancies resulting from the application of the site-specific approach increases from 0.15–0.35 at the first trigger to 0.45–0.6 after the fourth trigger. Beyond that point the magnitude discrepancies decrease slowly.

If we were to adopt a minimum of four stations real-time hypocentre determination algorithm, the time of the earliest alert we could issue would be about 18 s after the earthquake origin time (including the 3 s it takes to process the magnitude proxies, but not including network latency). This implies an unacceptably large blind-zone, leaving Jerusalem, Amman, Jericho and other large cities without warning (Fig. 1). This result highlights the importance of densifying the existing ISN network and implementing real-time single or dual-station hypocentre determination scheme.

5 PROSPECTS OF AN ONSITE EEWS ALONG THE DST

EEWS may be classified as either regional or onsite systems; while the first are based on the *P*-phase attributes at four or more network stations, the latter uses a smaller number of stations deployed within the target site. Consequently, use of the regional approach results

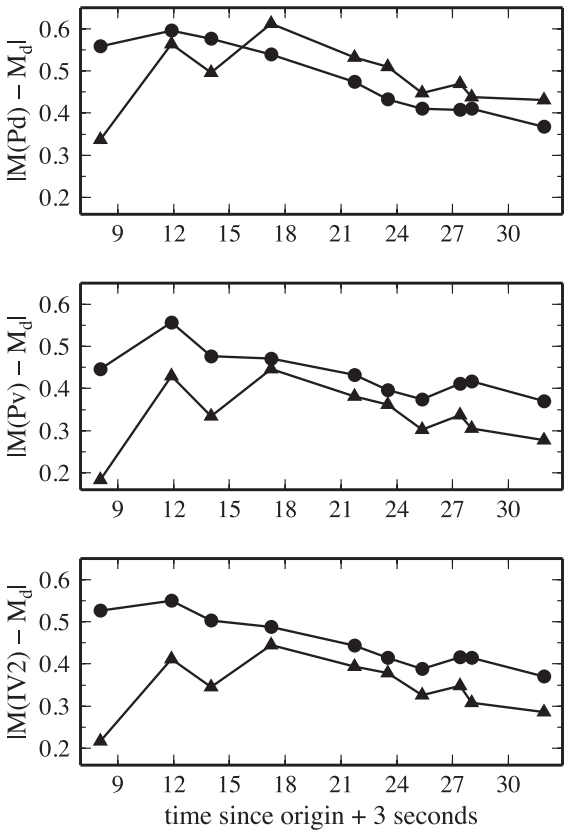

Figure 11. Average absolute magnitude discrepancy as a function of time with respect to the time of the Northern Dead Sea M_w 5.3 earthquake from 2004 February 11. Note that the time axis includes the 3 s it takes to process the magnitude proxies, but not the network latency. Magnitude discrepancies resulting from the application of the network-average and the site-specific empirical relations are indicated by circles and triangles, respectively.

in smaller rate of false and missed alarms than the onsite approach. Yet, a major disadvantage of the regional approach is that it results in a blind zone around the earthquake epicentre, whose radius depends on the network density. The dissemination of alert within that blind zone is either impossible, or is of little use due to a very short lead-time (i.e. the interval between the alert and the arrival of the strong ground shaking). Because, for example, Jerusalem is located within 25 km of the the damaging 1927, M_w 6.2, Jericho earthquake (Shapira *et al.* 1993), use of the ISN network *P*-wave approach alone will most likely fail to provide a useful warning in the event of another major earthquake near the hypocentre of that earthquake.

In Section 3, we show that correlations between amplitude-based magnitude proxies and catalogue magnitude at individual stations are strong. This is particularly the case for stations that are located very close to the DST (e.g. stations HMDT, DSI and ZFRI in Figs 3–5). Because amplitude-based proxies are subject to distance correction, it is concluded that earthquake magnitude may be determined rapidly and accurately using the first few seconds of *P*-wave waveforms recorded at individual stations along the DST, provided that onsite source–receiver distance determination is feasible. Several real-time hypocentre determination approaches may be considered (Satriano *et al.* 2010; Brown *et al.* 2011). The constraints on the onsite source–receiver distance are a function of network density. Thus, given the sparseness of the current ISN, the implementation of real-time hypocentre determination is expected to be ineffective. It is, however, extremely important that real-time hypocentre determination be tested once the new network configuration is set.

To enable onsite hypocentre determination along the DST, we have installed a small-aperture seismic array next to the DSI station (Fig. 1) that consists of a central three-component broad-band station surrounded by a set of six short period sensors. The maximum aperture between sensors is about 200 m. In general, use of a single array for epicentre determination is expected to yield better results than a single station determination, since the SNR can be increased by signal stacking (in proportion to the square root of the number of sensors), and since use of time delays at six different sensors should yield a better constrained backazimuth. We plan to install additional such arrays in the vicinity of ISN stations HMDT, MZDA and ZFRI (Fig. 1).

6 SUMMARY AND CONCLUSIONS

We examined the accuracy of rapid earthquake magnitude determination using an off-line data set of 95 earthquakes along the DST and South Lebanon that were recorded by 25 stations of the ISN between 2003 and 2011. We compared the correlation between five different real-time magnitude proxies and the catalogue magnitude. The five magnitude proxies that were considered in this study are the peak displacement, the peak velocity, the integral of the velocity squared, the predominant period and the characteristic period. All proxies were computed from the first 3 s of the *P*-phase vertical velocity component after being low-pass filtered at 3 Hz. In addition, the calculation of the three amplitude-based magnitude proxies was preceded by a one-over-distance rescaling of the velocity record.

We established site-specific empirical relations between each proxy and the catalogue magnitude. We then inferred similar relations for the entire network, after disregarding data recorded at stations for which the site-specific correlation was poor ($r < 0.85$). Given the magnitude range ($2.5 < M < 5.2$) that is available for the magnitude proxy calibration, amplitude-based magnitude proxies are more suitable than the frequency-based proxies for rapid magnitude determination in Israel and adjacent areas. We showed that use of site-specific empirical relations between amplitude-based magnitude proxies and catalogue magnitude can increase the accuracy of real-time magnitude estimations. We demonstrated that site-specific relations between amplitude-based magnitude proxies and catalogue magnitude at several stations along the DST are particularly robust, and thus conclude that data from individual stations or a couple of adjacent stations along the DST can be used to provide accurate earthquake alert, provided that real-time source–receiver distance determination is feasible.

Finally, while this study utilizes off-line data of limited magnitude range, its results clearly indicate that rapid earthquake magnitude determination in Israel and adjacent areas is feasible and can be incorporated effectively into an EEW algorithm. Owing to the short distances between major population centres and seismically active faults, the implementation of real-time single or dual-station source–receiver distance determination scheme is critical.

ACKNOWLEDGEMENTS

Data used in this study were provided by the seismological devision of the GII. We thank B. Reich, A. Polozov and N. Perelman of the GII for their assistance. This research was supported by the Ministry of Energy and Water Resources grant ES-51-2012. We thank the Editor, Jeannot Trampert, and the reviewers for their constructive remarks.

REFERENCES

Aki, K., 1967. Scaling law of seismic spectrum, *J. geophys. Res.,* **72,** 1217–1231.

Allen, R.M. & Kanamori, H., 2003. The potential for earthquake early warning in Southern California, *Science,* **300,** 786–789.

Allen, R.M., Gasparini, P., Kamigaichi, O. & Böse, M., 2009. The status of earthquake early warning around the world: an introductory overview, *Seismol. Res. Lett.,* **80,** 682–693.

Allen, R.M., Baer, G., Clinton, J., Hamiel, Y., Hofstetter, R., Pinsky, V., Ziv, A. & Zollo, A., 2012. Earthquake early warning for Israel: recommended implementation strategy, *Isr. Geol. Surv. Rep.,* GSI/26/2012.

Al-Tarazi, E., Abu-Rajab, J., Gomez, F., Cochran, W., Jaafar, R. & Ferry, M., 2011. GPS measurements of near-field deformation along the southern Dead Sea Fault System, *Geochem. Geophys. Geosyst.,* **12,** Q12021, doi:10.1029/2011GC003736.

Ambraseys, N.N. & Karcz, I., 1992. The earthquake of 1546 in the holy land, *Terra Nova,* **4**(2), 254–263.

Avni, R., 1999. The 1927 Jericho earthquake, comprehensive macroseismic analysis based on contemporary sources, *PhD thesis,* Ben-Gurion Univ. of the Negev, Beer Sheva, Israel (in Hebrew with English abstract).

Ben-Avraham, Y. & Ginzburg, A., 1990. Displaced terranes and crustal evolution of the Levant and the eastern Mediterranean, *Tectonics,* **9,** 613–622.

Ben-Menahem, A., Nur, A. & Vered, M., 1976. Tectonics, seismicity and structure of the Afro-Eurasian junction: the breaking of an incoherent plate, *Phys. Earth planet. Inter.,* **12,** 1–50.

Beroza, G.C. & Ellsworth, W.L., 1996. Properties of earthquake nucleation phase, *Tectonophysics,* **261,** 209–227.

Böse, M. *et al.*, 2013. CISN ShakeAlert: an earthquake early warning demonstration system for California, in *Early Warning for Geological Disasters: Scientific Methods and Current Practice,* pp. 49–69, eds Wenzel, F. & Zschau, J., Springer.

Brown, H.M., Allen, R.M., Hellweg, M., Khainovski, O., Neuhauser, D. & Souf, A., 2011. Development of the ElarmS methodology for earthquake early warning: realtime application in California and offline testing in Japan, *Soil Dyn. Earthq. Eng.,* **31,** 188–200.

Ellsworth, W.L. & Beroza, G.C., 1995. Seismic evidence for earthquake nucleation phase, *Science,* **268,** 851–855.

Eyal, M., Eyal, Y., Bartov, Y. & Steinitz, G., 1981. The tectonic development of the western margin of the Gulf of Elat (Aqaba) rift, *Tectonophysics,* **80,** 39–66.

Festa, G., Zollo, A. & Lancieri, M., 1986. Earthquake magnitude estimation from early radiated energy, *Geophys. Res. Lett.,* **35,** L22307, doi:10.1029/2008GL035576.

Garfunkel, Z., 1981. Internal structure of the Dead Sea leaky transform (rift) in relation to plate kinematics, *Tectonophysics,* **80,** 81–108.

Hamiel, Y., Amit, R. & Begin, Z.B., 2009. The seismicity along the Dead Sea Fault during the last 60,000 years, *Bull. seism. Soc. Am.,* **99**(3), 2020–2026.

Hamiel, Y., Baer, G., Allen, R.M., Clinton, J., Hofstetter, R., Pinsky, V., Ziv, A. & Zollo, A., 2013. Earthquake early warning for Israel: recommended implementation strategy, in *Proceedings of EGU General Assembly Conference Abstracts 15,* Vienna, Austria, EGU2013-4358.

Heaton, T.H., 1985. A model for a seismic computerized alert network, *Science,* **228,** 987–990.

Hofstetter, A., Fedman, L. & Rotstein, Y., 1991. Crustal structure of Israel: constraints from teleseismic and gravity data, *Geophys. J. Int.,* **104,** 371–379.

Iio, Y., 1992. Slow initial phase of P-wave velocity pulse generated by microearthquakes, *Geophys. Res. Lett.,* **19,** 477–480.

Iio, Y., 1995. Observations of slow initial phase generated by microearthquakes: implications for earthquake nucleation and propagation, *J. geophys. Res.,* **100,** 15 333–15 349.

Joffe, S. & Garfunkel, Z., 1987. Plate kinematics of the circum Red Sea: a re-evaluation, *Tectonophysics,* **141,** 5–22.

Lancieri, M., Fuenzalida, A., Ruiz, S. & Madariaga, R., 2011. Magnitude scaling of early-warning parameters for the Mw 7.8 Tocopilla, Chile, earthquake and its aftershocks, *Bull. seism. Soc. Am.,* **101**(2) 447–463.

Le Beon, M. *et al.*, 2008. Slip rate and locking depth from GPS profiles across the southern Dead Sea Transform, *J. geophys. Res.,* **113,** doi:10.1029/2007JB005280.

Lewis, M.A. & Ben-Zion, Y., 2007. Examination of scaling between proposed early signals in P waveforms and earthquake magnitudes, *Geophys. J. Int.,* **171,** 1258–1268.

Lockman, A.B. & Allen, R.M., 2005. Single-station earthquake characterization for early warning, *Bull. seism. Soc. Am.,* **95**(6), 2029–2039.

Marco, S., Rockwell, T., Heimann, A., Frieslander, U. & Agnon, A., 2005. Late Holocene activity of the Dead Sea Transform revealed in 3D palaeoseismic trenches on the Jordan Gorge segment, *Earth planet. Sci. Lett.,* **234,** 189–205.

Nakamura, Y., 1988. On the urgent earthquake detection and alarm system (UrEDAS), in *Proceedings of Ninth World Conference on Earthquake Engineering,* Vol. VII, pp. 673–678, Tokyo-Kyoto, Japan.

Olson, E.L. & Allen, R.M., 2005. The deterministic nature of earthquake rupture. *Nature,* **438,** 212–215.

Olson, E.L. & Allen, R.M., 2006. Is earthquake rupture deterministic? (Reply), *Nature,* **442**(E6), doi:10.1038/nature04964.

Rydelek, P. & Horiuchi, S., 2006. Is earthquake rupture deterministic? *Nature,* **442,** E5–E6.

Sadeh, M., Hamiel, Y., Ziv, A., Bock, Y., Fang, P. & Wdowinski, S., 2012. Crustal deformation along the Dead Sea Transform and the Carmel Fault inferred from 12 years of GPS measurements, *J. geophys. Res.,* **117,** B08410, doi:10.1029/2012JB009241.

Satriano, C., Elia, L., Martino, C., Lancieri, M., Zollo, A. & Iannaccone, G., 2010. PRESTo, the earthquake early warning system for Southern Italy: concepts, capabilities and future perspectives, *Soil Dyn. Earthq. Eng.,* **31,** doi:10.1016/j.soildyn.2010.06.008.

Shapira, A., Avni, R. & Nur, A., 1993. A new estimate for the epicenter of the Jericho earthquake of 11 July 1927, *Isr. J. Earth Sci.,* **42,** 93–96.

Shieh, J.T., Wu, Y.M. & Allen, R.M., 2008. A comparison of τ_c and τ_p^{max} for magnitude estimation in earthquake early warning, *J. geophys. Res.,* **35,** L20301, doi:10.1029/2008GL035611.

Wells, D.L. & Coppersmith, K.J., 1994. New empirical relationships among magnitude, rupture length, rupture width, rupture area and surface displacement, *Bull. seism. Soc. Am.,* **84,** 974–1002.

Wolfe, C.J., 2006. On the properties of predominant-period estimators for earthquake early warning, *Bull. seism. Soc. Am.,* **96**(5), 1961–1965.

Wu, Y.M. & Kanamori, H., 2005. Experiment on an onsite early warning method for the Taiwan early warning system, *Bull. seism. Soc. Am.,* **95**(1), 347–353.

Wu, Y. M. & Zhao, L., 2006. Magnitude estimation using the first three seconds P-wave amplitude in earthquake early warning, *Geophys. Res. Lett.,* **33,** L16312, doi:10.1029/2006GL026871.

Wurman, G., Allen, R.M. & Lombard, P., 2007. Toward earthquake early warning in northern California, *J. geophys. Res.,* **112,** B08311, doi:10.1029/2006JB004830.

Zollo, A., Lancieri, M. & Nielsen, S., 2006. Earthquake magnitude estimation from peak amplitudes of very early seismic signals on strong motion records, *Geophys. Res. Lett.,* **33,** L23312, doi:10.1029/2006GL027795.

SUPPORTING INFORMATION

Additional Supporting Information may be found in the online version of this article:

Table S1. Earthquakes analyzed in this study.

Figure S1. The logarithm of τ_c as a function of the catalog magnitude (*Md*) at individual stations. Green and blue symbols indicate earthquakes belonging to the 2008 Southern Lebanon swarm and the 2004 Dead Sea aftershock sequence, respectively, and the black symbols indicate events that occurred along the DST between 2003 and 2011. The solid lines are the linear least-square fit, with the correlation coefficient indicated at the top-left corner of each panel.

Figure S2. The logarithm of τ_p as a function of the catalog magnitude (*Md*) at individual stations. Green and blue symbols indicate earthquakes belonging to the 2008 Southern Lebanon swarm and the 2004 Dead Sea aftershock sequence, respectively, and the black symbols indicate events that occurred along the DST between 2003 and 2011. The solid lines are the linear least-square fit, with the correlation coefficient indicated at the top-left corner of each panel.

(http://gji.oxfordjournals.org/lookup/suppl/doi:10.1093/gji/ggt407/-/DC1).

Please note: Oxford University Press is not responsible for the content or functionality of any supporting materials supplied by the authors. Any queries (other than missing material) should be directed to the corresponding author for the article.